nature chemistry

SUPPLEMENTARY INFORMATION

DOI: 10.1038/NCHEM.1934

Genetically encoded reporters for hyperpolarized xenon magnetic resonance imaging

Mikhail G. Shapiro*, R. Matthew Ramirez, Lindsay J. Sperling, George Sun, Jinny Sun, Alexander Pines, David V. Schaffer, Vikram S. Bajaj*
*mikhail@caltech.edu, vikbajaj@gmail.com

Contents:

1. Detailed Methods

Cyanobacterial and halobacterial cell culture

Microcystis sp. (CCAP strain 1450/13) and *Anabaena flos-aquae* (CCAP strain 1403/13F) were purchased from CCAP (Argyll, Scotland, UK) and cultured in sterile BG11 and Gorham's algal media, respectively, at room temperature under office fluorescent lighting with an approximately 75% circadian duty cycle. *Halobacteria NRC-1* were purchased from Carolina Biological Supply (Burlington, NC) and cultured at 37°C in ATCC medium 2185, under ambient light, with shaking at 100-120 rpm.

GV isolation

GVs were isolated from *Anabaena flos-aquae* using hypertonic lysis and centrifugally-assisted flotation. Cells were concentrated over a 0.2μm filter and resuspended in TMC buffer (10mM Tris-HCl, 2.5mM $MgCl_2$, 0.5mM $CaCl_2$, pH7.6). A 1:1 volume of 50% sucrose was added rapidly and the cells incubated at room temperature for at least 30min. The solution was overlaid with a small volume of TMC and centrifugated overnight at 300rcf. GVs were harvested from the top of the solution. To achieve greater purity, the harvested GVs were resuspended in 10:1 TMC and re-centrifugated and harvested as above; this cycle was repeated 3 times. GVs from *Halobacteria NRC-1* were isolated by concentrating the cells through extended flotation, hypotonic lysis with 10:1 TMC, followed by centrifugally assisted flotation as described above. GVs were diluted to experimental concentrations using TMC. To prepare collapsed GVs, GV solutions were loaded into capped plastic syringes and the plunger depressed several times until the solution became translucent.

Measurement of GV concentration

The concentration of gas vesicles (GVs) isolated from *A. flos-aquae* was estimated based on pressure-sensitive OD at 500nm ($OD_{500,PS}$) due to intact GV light scattering, measured as the difference in optical density between a solution of intact GVs and the same solution of GVs after popping them through pressure application in a syringe. OD measurements were carried out on the NanoDrop ND-1000 spectrophotometer (Thermo Scientific, Wilmington, DE) with a path length of 1mm and scaled to 1cm. The relationship between $OD_{500,PS}$ and protein concentration (in mg/mL) was determined empirically using the BCA protein assay. Literature-based estimates of the molecular weight of the GVs (93MDa – 121MDa) [1, 2] were used to calculate the molar

concentration. We obtained a value of 564.2 ± 94.2 pM/ $OD_{500,PS}$, which we rounded up to 600 pM/ $OD_{500,PS}$. This value is slightly higher than ~450 pM/ $OD_{500,PS}$ which can be calculated from literature, the discrepancy possibly arising from incomplete GV purity, the presence of collapsed GVs in the OD measurement and/or differences in the protein assays used. The quantity of GVs purified from *Halobacteria NRC-1* was also measured and is reported in units of $OD_{500,PS}$.

Genetic modification and GV expression in *E. coli*

The pNL29 region of the *B. megaterium* gene cluster containing gvpB through gvpU (gift of Maura Cannon, University of Massachusetts at Amherst) was cloned into the pST39 plasmid for expression under control of the T7 promoter. pNL29-pST39 was transformed into BL21 DE3 *E. coli*. For tightly regulated IPTG-inducible expression the cells also contained a pLysE plasmid. For saturation spectroscopy and multiplexed imaging, transformed cells without pLysE were grown overnight at 30°C in selective LB media. For imaging and spectroscopic measurement of gene expression, transformed cells containing pLysE were induced with the indicated concentration of IPTG at OD_{600}~0.4 and grown overnight at 30°C. If necessary, prior to experiments cells were concentrated to the specified OD_{600} using a 0.2μm filter.

Mammalian cell culture and labeling

SKBR3 cells (ATCC, Manassas, VA) were cultured in McCoy's 5A medium supplemented with 10% fetal bovine serum (FBS), 100 I.U./ml penicillin and 100μg/ml streptomycin (pen/step). Before labeling, approximately $5x10^7$ cells were trypsinized and washed twice in phosphate buffered saline (PBS) and once in PBS with 2% bovine serum albumin (BSA). Jurkat T-cells (ATCC) were cultured in RPMI medium supplemented with 10% FBS and pen/strep. Before labeling, approximately $5x10^7$ Jurkat cells were harvested by centrifugation and washed as described for SKBR3 cells. A mouse monoclonal antibody against the human Her2/ERBB2 receptor (clone N12, Thermo Scientific, Fremont, CA) was functionalized with streptavidin using the Lightning-Link Streptavidin Conjugation kit following supplier instructions. Purified GVs from *A. flos-aquae* were biotinylated using EZ-Link Sulfo-NHS-LC-biotin (Thermo Scientific, Rockford, IL) following supplier instructions and purified by flotation. Streptavidin antibodies were conjugated to biotin-GVs overnight at 4°C at a 1:4 w/w ratio. To label cells, antibody-conjugated GVs in PBS with 2% BSA were mixed with cells at a GV concentration (based on $OD_{500,PS}$) of approximately 400pM. After 1 hour at 4°C, cells were washed twice with PBS and resuspended in 0.6mL PBS for imaging and spectroscopy.

HyperCEST NMR

Hyperpolarized xenon was prepared by spin-exchange optical pumping using a homebuilt polarizing apparatus. Briefly, a gas mixture (2% Xe natural abundance, 10% N_2, 88% He) was flowed continuously through the optical pumping cell, which contained approximately 1 g of Rb metal and was heated to produce a vapor. The Rb vapor was irradiated with a circularly polarized infrared laser (λ = 795 nm) to polarize its valence electron, and this electronic polarization was transferred to ^{129}Xe upon colliding with Rb via hyperfine coupling. After polarization (~2%), the gas mixture was delivered to the phantom, an NMR tube (d=5mm or 10mm) modified with inlet and outlet ports, through plastic tubing and dissolved in the sample by bubbling through a capillary or set of capillary tubes. Bubbling was controlled using TTL pulses built into the pulse sequence, which in turn controlled pneumatic valves that routed the polarized gas either through the phantom or around it. A 10 second bubble period was followed

by a 5 second wait period to allow bubbles to dissipate and the solution to settle. Gas flow rates varied between 0.15 SLM and 0.3 SLM. The entire system, including the phantom, was sealed under a total gas pressure of 1.57 atm to 1.7 atm.

^{129}Xe NMR and MRI was performed at 9.4 T on a Varian spectrometer (Palo Alto, CA). All experiments were conducted at room temperature, and chemical shifts were referenced to the gaseous ^{129}Xe signal. Data were collected using commercial, dual-tuned (^{1}H, broadband) 5 mm and 10mm probes. For saturation contrast, continuous wave (cw) radiofrequency (RF) pulses with offset frequencies, field strengths and durations specified in Supplementary Table 1 were applied after the wait period and prior to excitation. Frequency-dependent saturation spectra were obtained by measuring the aqueous ^{129}Xe signal as a function of saturation pulse offset, varying from -77.2 ppm to 284.4 ppm in 101 steps. All offsets are relative to ^{129}Xe gas.

After data collection, raw FIDs were processed in MATLAB (The MathWorks, Natick, MA) by first applying 10 Hz Lorentzian apodization in the time domain before Fourier transform and phase correction. The area of the aqueous ^{129}Xe resonance was integrated, and this value was considered for later analyses. To compute saturation contrast, the mean on-resonance signal was subtracted from the mean off-resonance signal ($N \geq 5$) under each condition, and the resulting difference was normalized to the mean off-resonance signal. Data and error bars in figures represent the means and standard errors of measurement of biological replicates, with replicate numbers (N) listed in figure captions.

For imaging, a custom phantom was fabricated comprising three 5-mm NMR tubes packed together side-by-side to form a triangle, and fitted with inlet and outlet ports to connect the gas flow from the xenon polarizer. This phantom fit inside of the 10-mm NMR probe. Xenon images were acquired using a fast spin echo imaging sequence, modified to incorporate bubbling and wait periods, as well as a saturation pulse prior to excitation with a 2 ms sinc pulse. Bubbling typically lasted 10 s followed by a 2.5 s wait period, except for experiments with mammalian cells, which used a 7 s bubble and 4 s wait to minimize foaming. Total gas pressure was maintained between 1.46 atm and 1.57 atm, and the flow rate was either 0.2 SLM or 0.25 SLM.

A train of 8 echoes was used with echo time (TE) of 10 ms, and an overall repetition time (TR) of either 17.58 s (for acquisitions with 7 s bubble and 4 s wait), or 19.08 s (for 10 s bubble and 2.5 s wait). RF saturation was applied immediately after the wait time. Saturation parameters and image averages are listed in Supplementary Table 2. Signals were acquired with a 12.02 kHz spectral width and 2.66 ms acquisition time. All images were axial without slice-selection, and the k space matrix consisted of 32 points in the readout dimension and 16 phase encoding points. The field of view was 20 mm by 20 mm. The raw matrix was zero-filled by a factor of two in each dimension, manually re-centered in k space, and apodized with a symmetric 2D Gaussian (FWHM = 6 cm^{-1}) before 2D Fourier transform to generate images. The root mean square (RMS) noise signal was calculated for a 5 mm by 5 mm square region and images were thresholded starting at 3 times the RMS noise.

Proton images were also acquired with a fast spin echo imaging sequence (TR = 1.5 s, TE = 16.7 ms, 4 echoes per excitation) after 2 ms sinc excitation, no slice-selection, and 192 points in both readout and phase encode dimensions over a 20 mm by 20 mm field of view. Signals were acquired with a 20.16 kHz spectral width and 9.52 ms acquisition time. The k space matrix was zero-filled once prior to two-dimensional Fourier transform in MATLAB. All proton images are result of 4 averages.

Xenon saturation contrast maps were produced by comparing off-resonance and on-resonance ^{129}Xe saturation images (Supplementary Fig. 7) voxel-by-voxel using custom scripts in MATLAB. The scripts first subtracted the on-resonance saturation image from the off-resonance saturation image to produce a difference image, which was subsequently divided by the off-resonance saturation image thereby normalizing the change in signal. Off-resonance images were used to define regions of interest (ROIs), and the final Xe saturation contrast maps reflect only the contrast within these ROIs. Dashed outlines of the ROIs are overlaid on images as a visual aide.

Transmission electron microscopy (TEM)

TEM images were obtained on a Philips/FEI (Hillsboro, OR) Tecnai 12 microscope operating at 120kV. GV samples were negatively stained with 2% uranyl acetate and deposited on a carbon-coated formvar grid. Thin section TEM *E. coli* specimens were prepared by fixing the cells in glutaraldehyde, osmium tetroxide and ferrous cyanide, dehydrating in acetone, embedding in epoxy resin and sectioning under ambient pressure.

2. Supplementary Tables S1-S4

Supplementary Table S1 – RF saturation parameters used in HyperCEST spectroscopy.

Fig.	Specimen(s)	Phantom diameter (mm)	Power (μT, Hz)	Dura-tion (s)	On-resonance (ppm)	Off-resonance (ppm)
1b	400pM GVs	5	33.6, 396	0 to 6.5	31.2	n/a
1c	Intact and collapsed GVs, 400pM	5	16.9, 199	6.5	Spectrum	n/a
1e	GVs at 0 to 400pM	5	33.6, 396	0 to 6.5	31.2	356.7
2a	(i) *Microcystis sp.* (ii) *Halobacteria NRC-1* (iii) *E. coli*	10	(i)13.5, 159 (ii)12.9, 152 (iii)14.6, 172	6.5	Spectrum	n/a
3c	E. coil containing pNL29 + quantities of IPTG	10	30.1, 354	6.5	58.6	338.3
3f	GV-labeled SKBR3 and Jurkat cells	5	23.2, 273	6.5	31.2	356.7

Supplementary Table S2 – RF saturation and averaging parameters used in HyperCEST imaging.

Fig.	Specimen(s)	Power (μT, Hz)	Duration (s)	On-resonance (ppm)	Off-resonance (ppm)	Averages per image
1f	0pM, 100pM, 400pM GVs	26.9, 317	6.5	31.2	356.7	48
2b	*Microcystis sp.*, *Halobacteria NRC-1*, *E. coli pNL29*	21.3, 251	6.5	9.0	329.9	16
2c	*Microcystis sp.*, *Halobacteria NRC-1*, *E. coli pNL29*	21.3, 251	6.5	30.6	329.9	16

2d	*Microcystis sp.*, *Halobacteria NRC-1*, *E. coli pNL29*	21.3, 251	6.5	58.6	329.9	16
3a	*E. coil* pNL29 +/- IPTG, Control *E. coli* + IPTG	25.8, 304	6.5	51.2	338.3	48
3e	GV-labeled SKBR3 and Jurkat cells	23.2, 273	6.5	31.2	356.7	16

Supplementary Table S3 – Pharmacokinetic model parameters

Symbol	Parameter	Value	Source
V_l	Lung volume[i]	3 mL	Zhou et al.[3]
V_m	Mouth and trachea volume	1 mL	Visual estimate
f_p	Pulmonary blood flow[ii]	1.2 mL sec^{-1}	Austgen et al.[4]
f_b	Cerebral tissue blood flow	1 L min-1 L^{-1}	Norberg et al.[5]
p_b	Blood-brain partition coefficient	1.06	Gjedde et al. [6]
Θ	Ostwald coefficient for Xenon in blood	0.14	Martin et al.[7]
τ_b	Lung-brain transit[iii]	4 sec	Elderidge et al.[8]
f_r	Respiratory flow rate (in and out)[iv]	6 mL sec^{-1}	Zhou et al.[3]
T_{1r}	T1 time in gas reservoir	1000 sec	Martin et al.[7]
T_{1m}	T1 time in mouth	12 sec	Martin et al.[7]
T_{1l}	T1 time in lung	12 sec	Martin et al.[7]
T_{1a}	T1 time in arterial blood	6 sec	Martin et al.[7]
T_{1b}	T1 time in brain tissue	15 sec	Zhou et al.[3]
K_{sat}	HyperCEST on-resonance saturation rate[v]	0.33 sec^{-1}	Fig. 1e

Notes:
(i) For simplicity, we assume that the lung volume and the breath volume are the same and that the lung gets filled with new gas during each inhalation
(ii) Based on a body mass of 300 g
(iii) Value for rats could not be located in the literature; the cited value comes from a study in cats; the rat value is expected to be smaller based on anatomy, which would result in stronger overall xenon signals
(iv) Based on a breathing rate of 60 breaths min^{-1} and breath volume of 3 mL (Zhou et al.[3])
(v) Assuming local concentration of 400 pM *Ana* GVs

Supplementary Table S4 – Pharmacokinetic model variables

Symbol	Parameter	Initial value
C_r	Hyperpolarized xenon concentration in the gas reservoir	3.96 mM
C_m	Hyperpolarized xenon concentration in the mouth and trachea	0
C_l	Hyperpolarized xenon concentration in the lungs	0
C_p	Hyperpolarized xenon concentration in the pulmonary circulation	0
C_a	Hyperpolarized xenon concentration in brain arteries	0
C_b	Hyperpolarized xenon concentration in brain tissue	0

3. Supplementary Figures S1-S7

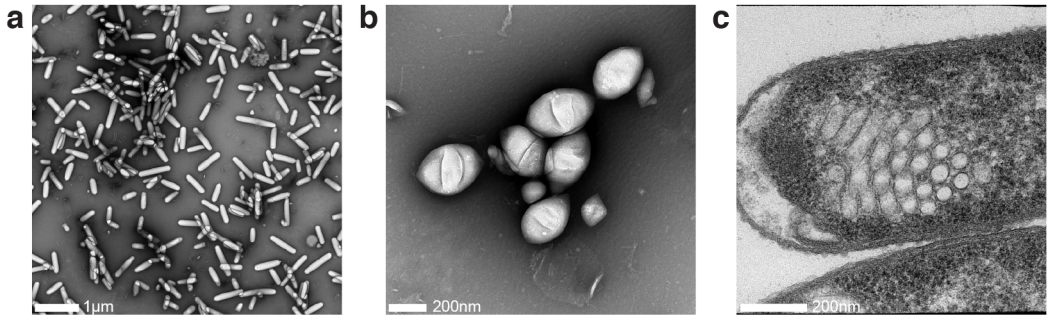

Supplementary Figure S1 – Additional transmission electron micrographs of GVs. (a) GVs purified from *Anabaena flos-aquae* imaged with TEM at a lower magnification compared to Fig. 1d. Note the absence of particulate contaminants. A small number of collapsed GVs is visible, which may be present in experimental samples or may result from GV collapse during TEM specimen preparation. **(b)** TEM of GVs purified from *Halobacteria NRC-1*. (**c**) Thin section TEM image of *E. coli* expressing the pNL29 gene cluster.

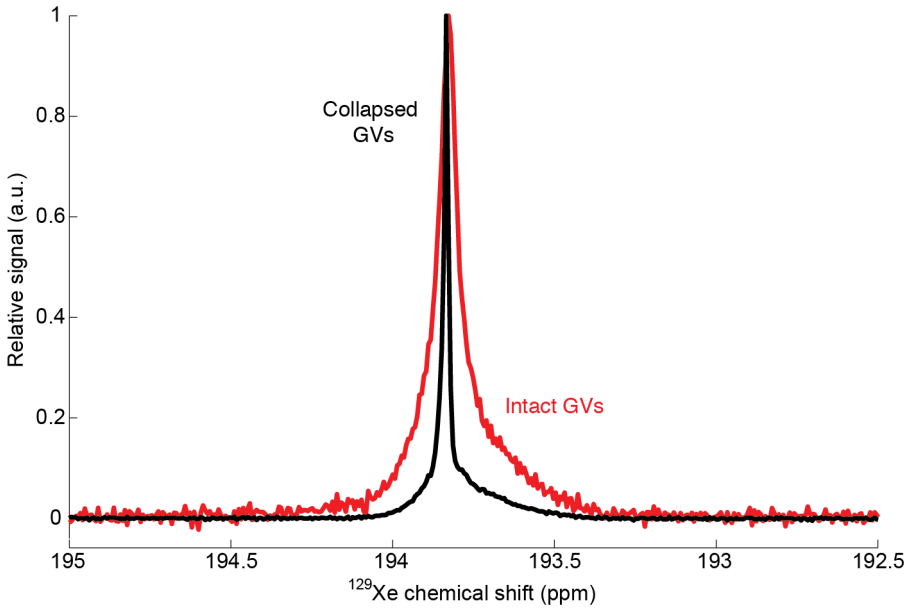

Supplementary Figure S2 – GVs broaden the spectral peak of ^{129}Xe. NMR spectra of ^{129}Xe in TMC buffer containing 400pM intact (red) or collapsed (black) *Anabaena flos-aquae* GVs. Each spectrum is normalized to its peak amplitude.

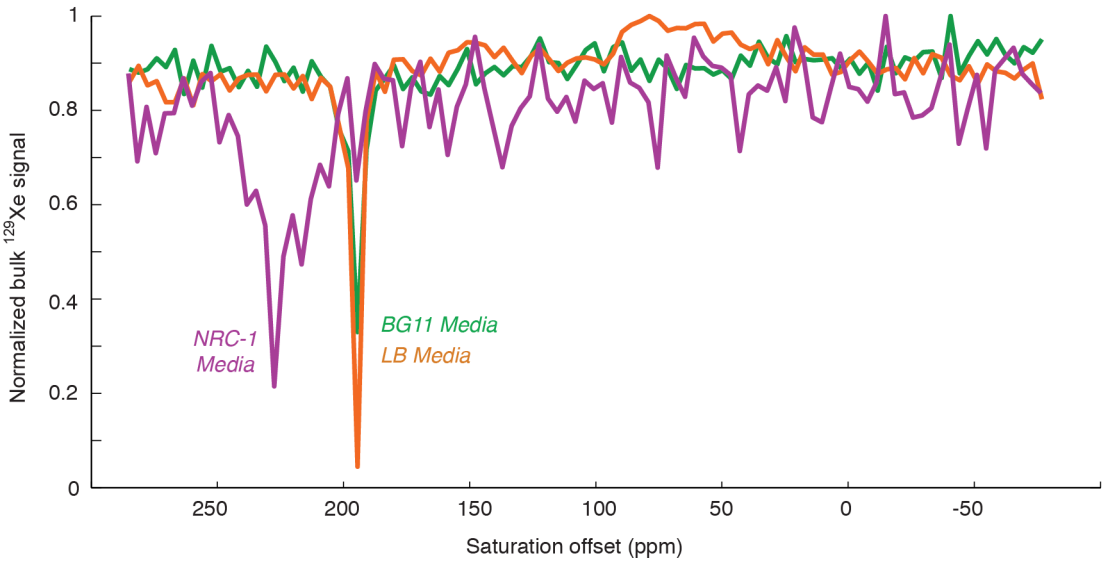

Supplementary Figure S3 – Saturation spectra of cell culture media. Frequency-dependent saturation spectra for NRC-1, BG11 and LB media, used to culture *Halobacteria NRC-1*, *Microcystis sp.* and *E. coli*, respectively, and present in the samples measured in Fig. 2. N=3 for NRC-1; N=1 for BG11 and LB. Saturation parameters were the same as used in Fig. 2a.

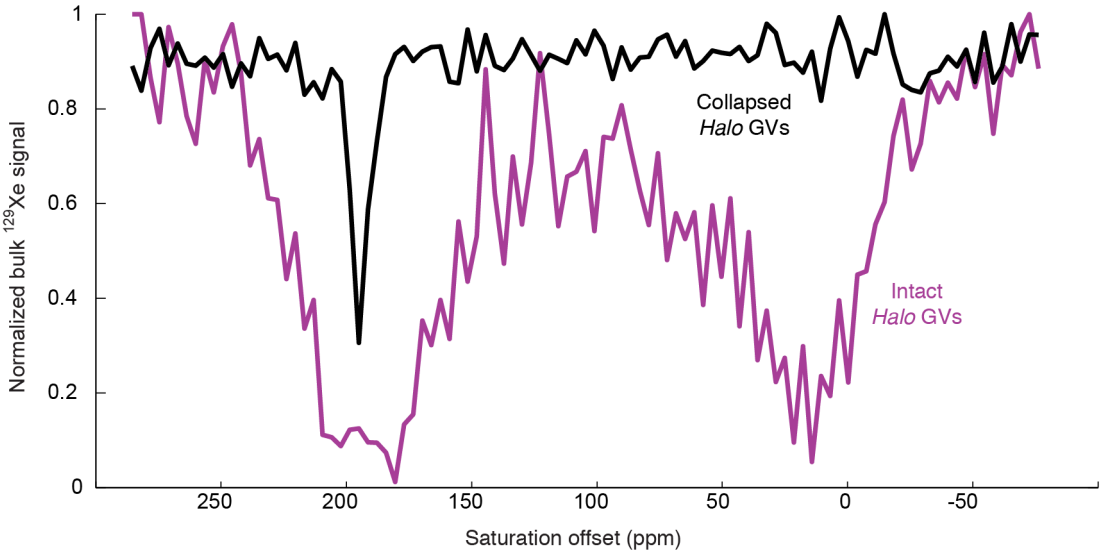

Supplementary Figure S4 - Saturation spectra of purified halobacterial GVs. Frequency-dependent saturation spectra for intact and collapsed GVs purified from from *Halobacteria NRC-1*. N=1. Note that the GV saturation peak at ~14.4 ppm matches that of intact *Halobacteria NRC-1* (Fig. 2a) but that aqueous Xe saturation is centered around 195 ppm, as in the GVs shown in Fig. 1c. The spectra are noisier than in other figures because lower pressure and gas flow rate had to be used due to the collapse fragility of *Halobacteria NRC-1* GVs. Saturation parameters were the same as used in Fig. 1c.

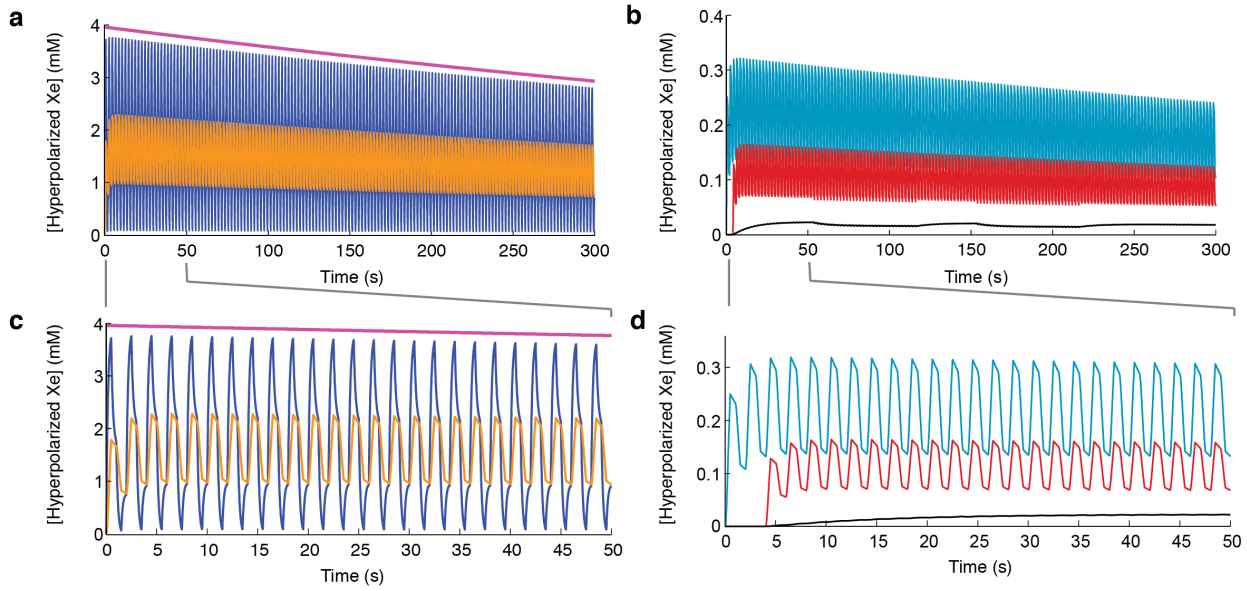

Supplementary Figure S5 – Hyperpolarized xenon distribution predicted by a pharmacokinetic model. Time course of the concentrations of hyperpolarized xenon in the gas reservoir (C_r, magenta), mouth (C_m, blue), lungs (C_l, orange) in panels **a** and **c**; pulmonary vein (C_p, cyan), cerebral arteries (C_a, red) and brain tissue (C_b, black) in panels **b** and **d**. Panels **a-b** show the results of the entire 300 second simulation. Panels **c-d** show the same data, but focused on the first 50 seconds during which C_b reaches steady state.

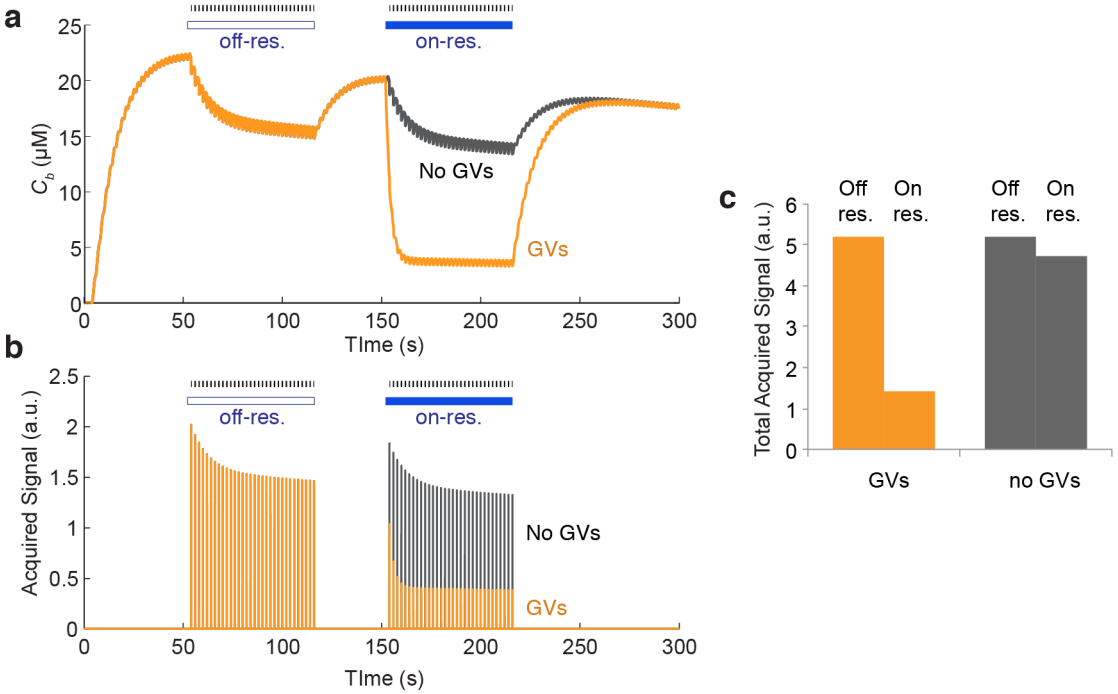

Supplementary Figure S6 – Brain concentrations of hyperpolarized xenon and MRI signals in HyperCEST imaging. (**a**) Predicted concentrations of hyperpolarized xenon (C_b) in brain tissue during a HyperCEST imaging sequence in brain regions containing (orange) or devoid of (gray) 400 pM GVs. Black tick marks indicate the timing of image acquisition pulses with flip angle α=20º. The hollow and solid blue bars indicate the timing of off-resonance and on-resonance (at the GV peak) saturation pulses, respectively; saturation is interleaved with image acquisition pulses. (**b**) Predicted MRI signal acquired from each imaging pulse in brain regions containing (orange) or devoid of (gray) 400 pM GVs. (**c**) Total signal acquired with and without saturation in brain regions containing (orange) or devoid of (gray) 400 pM GVs.

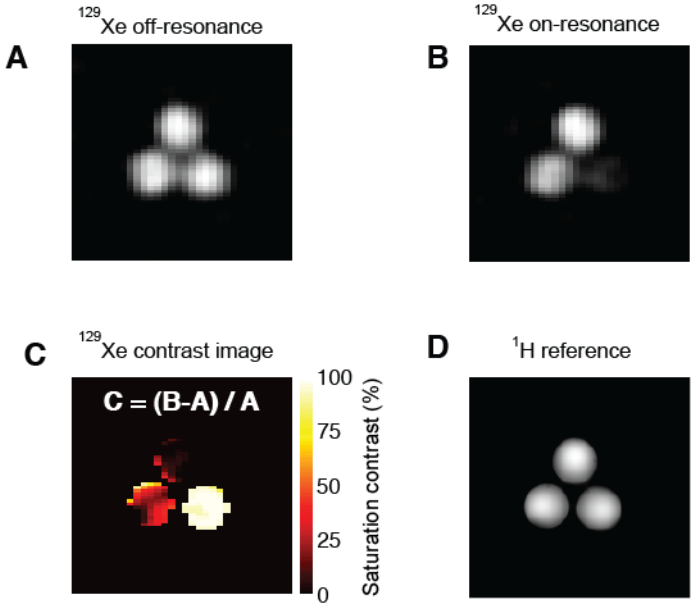

Supplementary Figure S7. Example of image processing resulting in HyperCEST saturation contrast images. Raw ^{129}Xe images with off-resonance (**A**) and on-resonance (**B**) saturation. (**C**) ^{129}Xe contrast image (same as Fig. 1F) generated by subtracting (B) from (A) and normalizing voxel-by-voxel by (A), resulting in a per-voxel % saturation. All values in (C) that fall outside the phantom, defined using the off-resonance image in (A), are masked. (**D**) ^{1}H reference image of the phantom shown in (A)-(D).

4. Pharmacokinetic Model of HyperCEST imaging *in vivo*

To assess the feasibility of HyperCEST imaging *in vivo*, we implemented a previously published pharmacokinetic model of inhaled hyperpolarized xenon aimed at estimating cerebral tissue concentrations of polarized nuclei[7]. Model parameters were adjusted to represent rat experimental subjects[3], and combined with a simulated saturation and imaging pulse sequence to determine its ability to detect the presence of 400 pM GVs in brain tissue. The parameters and variables used in our model implementation are listed in Supplementary Tables 3 and 4. Equations 1-8 were integrated in MATLAB using the Euler method for 300 seconds using time steps of 10 ms.

$$\frac{dC_r}{dt} = -\frac{C_r}{T_{1r}} \qquad (1)$$

$$\frac{dC_m}{dt} = -\frac{C_m}{T_{1m}} + \frac{f_{b,in}}{V_m}\left(C_r - C_m\right) \quad \text{(inhalation)} \qquad (2)$$

$$\frac{dC_m}{dt} = -\frac{C_m}{T_{1m}} + \frac{f_{b,out}}{V_m}\left(C_{lung} - C_m\right) \quad \text{(exhalation)} \qquad (3)$$

$$\frac{dC_l}{dt} = -\frac{C_l}{T_{1l}} + \frac{f_{b,in}}{V_l}\left(C_m - C_l\right) - \frac{f_p \Theta C_l}{V_l} \quad \text{(inhalation)} \qquad (4)$$

$$\frac{dC_l}{dt} = -\frac{C_l}{T_{1l}} - \frac{f_p \Theta C_l}{V_l} \quad \text{(exhalation)} \quad (5)$$

$$C_p = \Theta C_l \quad (6)$$

$$C_a(t) = C_p(t - \tau_b) - \exp\left(-\frac{\tau_b}{T_{1A}}\right) \quad (7)$$

$$\frac{dC_b}{dt} = f_b C_a - C_b\left(\frac{f_b}{p_b} + \frac{1}{T_{1b}} + K_{sat}\right) \quad (8)$$

The simulation assumed an initial reservoir concentration of 3.96 mM isotopically enriched hyperpolarized ^{129}Xe gas based on a Xe density of 5.15mg/ml (ref [7]) with 10% polarization. The gas is administered through alternating breaths of Xe and O_2 (ref [3]). The resulting relative concentrations of ^{129}Xe in each compartment resemble the results of Martin et al.[7] (Supplementary Fig. 5), with some differences in dynamics resulting from the assumption of alternating breaths of Xe/O_2 instead of continuous Xe and the use of a constant lung volume. The peak concentration of hyperpolarized ^{129}Xe in brain tissue is predicted to be 22.4 μM (Supplementary Fig. 5 b-d, Supplementary Fig. 6a). Using the assumptions of Martin et al[7], this results in a signal-to-noise ratio (SNR) 64-fold lower than that expected for thermally polarized protons based on equation 9, where γ_{Xe} and γ_H are the gyromagnetic ratios of ^{129}Xe and ^{1}H (11.77 and 42.577, respectively), C_H is the proton concentration (assumed to be 80 M) and the B_o field and temperature are taken to be 1.5 T and 310 K.

$$\frac{SNR_{Xe}}{SNR_H} = \frac{C_b \gamma_{Xe}}{C_H(\gamma_H^2 \hbar B_o / 2kT)} \quad (9)$$

In conjunction with the pharmacokinetics, we simulated a generalized CEST imaging pulse sequence, aiming to capture the effect of saturation and acquisition pulses on Xe polarization and estimate the relative acquired signal in the on-resonance and off-resonance conditions. The acquisition sequence contains 32 RF pulses with a flip angle α = 20º and a repetition time of 2 seconds. All pulses and signals are assumed to be localized to brain tissues and arteries, e.g., through the use of a surface coil. When C_b reaches a steady state approximately 50 seconds after the start of the experiment, the acquisition sequence is applied. Each pulse instantaneously reduces C_a and C_b by a factor of 1-cos(α), and the resulting signal is taken to be proportional to $(C_b+0.014C_a)\sin(\alpha)$, assuming the cerebral vasculature occupies 1.4% of brain volume[9]. After steady state polarization recovers, an imaging sequence is applied again, but is now interleaved with saturation pulses at a GV-selective frequency, starting 2 seconds before the imaging sequence. Saturation pulses result in a decrease in C_b at a rate K_{sat} = 0.33 sec^{-1} in GV-containing regions (equation 8), consistent with the CEST effect observed in the presence of 400 pM GVs using the saturation parameters of Fig. 1e. Saturation transfer reduces the concentration of polarized xenon (Supplementary Fig. 6a), and consequently the level of acquired signal (Supplementary Fig. 6b). No saturation using GV-specific frequencies is expected to occur in tissues lacking GVs. The total signal acquired during each imaging sequence is proportional to the sum of the signals produced during component individual pulses.

As shown in Supplementary Fig. 6c, tissues containing GVs are predicted to display saturation contrast (% change between the saturating and non-saturating acquisitions) of 73%. A

small change also appears in the non-GV condition due to the order of image acquisitions and slowly declining C_r, but this could be controlled for by reversing the order of saturating and non-saturating imaging sequences.

5. Supplementary References:

1. Jost, M., Jones, D.D. & Weathers, P.J. Counting of gas vacuoles by electron microscopy in lysates and purified fractions of microcystis aeruginosa. *Protoplasma*, 329-335 (1971).
2. Walsby, A.E. & Armstrong, R.E. Average thickness of the gas vesicle wall in Anabaena flos-aquae. *J Mol Biol* **129**, 279-285 (1979).
3. Zhou, X. et al. Reinvestigating hyperpolarized (129)Xe longitudinal relaxation time in the rat brain with noise considerations. *NMR Biomed* **21**, 217-225 (2008).
4. Austgen, T.R., Plumley, D.A. & Souba, W.W. Simple method of determining pulmonary blood flow in the anesthetized rat. *Investigative Surgery* **4**, 81-86 (1991).
5. Norberg, K. & Siesjö, B.K. Quantitative measurement of blood flow and oxygen consumption in the rat brain. *Acta Physiologica Scandinavica* **91**, 154-164 (1974).
6. Gjedde, A., Caronna, J.J., Hindfelt, B. & Plum, F. Whole-brain blood flow and oxygen metabolism in the rat during nitrous oxide anesthesia. *American Journal of Physiology--Legacy Content* **229**, 113-118 (1975).
7. Martin, C.C. et al. The pharmacokinetics of hyperpolarized xenon: implications for cerebral MRI. *J Magn Reson Imaging* **7**, 848-854 (1997).
8. Eldridge, F.L. & Millhorn, D.E. Oscillation, gating, and memory in the respiratory control system. *Comprehensive Physiology* (1986).
9. Cremer, J.E. & Seville, M.P. Regional brain blood flow, blood volume, and haematocrit values in the adult rat. *Journal of Cerebral Blood Flow & Metabolism* **3**, 254-256 (1983).